

Combined Therapy of AXL and HDAC Inhibition Reverses Mesenchymal Transition in Diffuse Intrinsic Pontine Glioma



Michaël H. Meel^{1,2}, Mark C. de Gooijer³, Dennis S. Metselaar^{1,2}, A. Charlotte P. Sewing¹, Kenn Zwaan¹, Piotr Waranecki^{1,2}, Marjolein Breur⁴, Levi C.M. Buil³, Tonny Lagerweij⁵, Laurine E. Wedekind⁵, Jos W.R. Twisk⁶, Jan Koster⁷, Rintaro Hashizume⁸, Eric H. Raabe⁹, Ángel Montero Carcaboso¹⁰, Marianna Bugiani⁴, Timothy N. Phoenix¹¹, Olaf van Tellingen³, Dannis G. van Vuurden^{1,2}, Gertjan J.L. Kaspers^{1,2}, and Esther Hulleman^{1,2}

ABSTRACT

Purpose: Diffuse intrinsic pontine glioma (DIPG) is an incurable type of pediatric brain cancer, which in the majority of cases is driven by mutations in genes encoding histone 3 (H3K27M). We here determined the preclinical therapeutic potential of combined AXL and HDAC inhibition in these tumors to reverse their mesenchymal, therapy-resistant, phenotype.

Experimental Design: We used public databases and patient-derived DIPG cells to identify putative drivers of the mesenchymal transition in these tumors. Patient-derived neurospheres, xenografts, and allografts were used to determine the therapeutic potential of combined AXL/HDAC inhibition for the treatment of DIPG.

Results: We identified AXL as a therapeutic target and regulator of the mesenchymal transition in DIPG. Combined AXL and HDAC inhibition had a synergistic and selective antitumor effect

on H3K27M DIPG cells. Treatment of DIPG cells with the AXL inhibitor BGB324 and the HDAC inhibitor panobinostat resulted in a decreased expression of mesenchymal and stem cell genes. Moreover, this combination treatment decreased expression of DNA damage repair genes in DIPG cells, strongly sensitizing them to radiation. Pharmacokinetic studies showed that BGB324, like panobinostat, crosses the blood–brain barrier. Consequently, treatment of patient-derived DIPG xenograft and murine DIPG allograft-bearing mice with BGB324 and panobinostat resulted in a synergistic antitumor effect and prolonged survival.

Conclusions: Combined inhibition of AXL and HDACs in DIPG cells results in a synergistic antitumor effect by reversing their mesenchymal, stem cell-like, therapy-resistant phenotype. As such, this treatment combination may serve as part of a future multimodal therapeutic strategy for DIPG.

¹Departments of Pediatric Oncology/Hematology, Cancer Center Amsterdam, Amsterdam University Medical Centers, Amsterdam, the Netherlands. ²Princess Máxima Center for Pediatric Oncology, Utrecht, the Netherlands. ³Division of Pharmacology/Mouse Cancer Clinic, The Netherlands Cancer Institute, Amsterdam, the Netherlands. ⁴Department of Pathology, Amsterdam University Medical Centers, Amsterdam, the Netherlands. ⁵Department of Neurosurgery, Neuro-oncology Research Group, Cancer Center Amsterdam, Amsterdam University Medical Centers, Amsterdam, the Netherlands. ⁶Department of Epidemiology and Biostatistics, Amsterdam University Medical Centers, Amsterdam, the Netherlands. ⁷Department of Oncogenomics, Amsterdam University Medical Centers, Amsterdam, the Netherlands. ⁸Departments of Neurological Surgery and Molecular Genetics, Northwestern University Feinberg School of Medicine, Chicago, Illinois. ⁹Division of Pediatric Oncology, Sidney Kimmel Comprehensive Cancer Center, Johns Hopkins University School of Medicine, Baltimore, Maryland. ¹⁰Preclinical Therapeutics and Drug Delivery Research Program, Department of Oncology, Hospital Sant Joan de Déu Barcelona, Spain. ¹¹Division of Pharmaceutical Sciences, College of Pharmacy, University of Cincinnati/Research in Patient Services, Cincinnati Children's Hospital Medical Center, Cincinnati, Ohio.

Note: Supplementary data for this article are available at Clinical Cancer Research Online (<http://clincancerres.aacrjournals.org/>).

Corresponding Author: Esther Hulleman, Heidelberglaan 25, 3584CS Utrecht, The Netherlands. Phone: +31 (0) 88 972 51 14; E-mail: e.hulleman@prinsesmaximacentrum.nl

Clin Cancer Res 2020;26:3319–32

doi: 10.1158/1078-0432.CCR-19-3538

©2020 American Association for Cancer Research.

Introduction

Diffuse intrinsic pontine glioma (DIPG) is a brain tumor that almost uniquely occurs in children and is universally fatal with a median survival of only 11 months (1). The poor prognosis of this cancer is related to its delicate location in the brainstem and its resistance to chemotherapy, caused by both intrinsic factors and the maintained integrity of the blood–brain barrier (BBB; ref. 2). On a molecular level, DIPG is characterized by a high prevalence (~80%) of specific mutations in histone 3 genes (mainly *H3F3A* and *HIST1H3B*). These mutations result in a lysine-to-methionine substitution on position 27 (H3K27M), thereby causing a dominant negative loss of methylation on H3K27 and aberrant transcription of oncogenes (3, 4).

Recent studies identified a mesenchymal gene expression signature in a subset of patients with DIPG that correlates with the presence of a *HIST1H3B* mutation, although this profile is not restricted to this subset of tumors (3, 5). In many other types of cancer, including adult glioblastoma (GBM), such a mesenchymal gene signature is associated with a process termed epithelial-to-mesenchymal transition (EMT), which is believed to be responsible for resistance to therapy, invasion, metastasis, and poor clinical outcome (4, 6, 7). Molecularly, the mesenchymal transition is often initiated by external factors, for example, hypoxia or growth factors, leading to upregulation of master transcriptional regulators, such as SNAIL/SLUG (SNAI1/SNAI2) and ZEB1, and repression of E-cadherin (4). Furthermore, expression of these transcriptional regulators has been associated with stem cell features in various types of cancer, including GBM (8–13).

Translational Relevance

Diffuse intrinsic pontine glioma (DIPG) is a highly aggressive and incurable pediatric brain tumor, for which no effective curative treatments are available. We show that reversal of the mesenchymal, therapy-resistant phenotype of DIPG cells by combined AXL/HDAC inhibition results in a synergistic antitumor effect and a strong sensitization of DIPG cells to radiation. This synergy was unique to cells carrying a H3K27M mutation, conferring selective toxicity to DIPG cells. Importantly, the AXL inhibitor BGB324 crosses the blood–brain barrier, allowing for effective treatment of DIPG xenograft- and allograft-bearing mice, in combination with the HDAC inhibitor panobinostat. As such, this combination treatment may form the backbone of a future multimodal therapeutic strategy for DIPG.

Here we identify AXL, a receptor tyrosine kinase (RTK) that has previously been described as an initiator of the mesenchymal transition in adult GBM (14–18), as a novel therapeutic target in DIPG.

We describe the preclinical development of a therapeutic strategy based on small molecule inhibition of AXL. For this purpose, we evaluated the *in vitro* and *in vivo* efficacy, as well as the mechanism of action and brain pharmacokinetics, of the specific AXL inhibitor BGB324 (bemcentinib; refs. 18, 19), which is currently under investigation in clinical trials for the treatment of adult malignancies. We further demonstrate the efficacy and biological effects of combining BGB324 with the pan-HDAC inhibitor panobinostat, a drug that has previously been identified as a potential therapeutic agent for DIPG (20), and is currently in a phase I clinical trial for children with recurrent disease (NCT02717455). In other types of cancer, panobinostat has been shown to reverse the mesenchymal transition via different mechanisms than BGB324, providing a biological rationale for combined treatment with AXL inhibition (21, 22). We finally determine the efficacy of the combination of BGB324, panobinostat, and fractionated radiation, for potential integration in the current standard therapeutic regimen. The results presented here indicate that the combination of BGB324 and panobinostat reverses the mesenchymal transition, as well as the resulting therapy resistance, thus forming a promising part of future multimodal therapeutic strategies for DIPG.

Materials and Methods

Cell lines and culture conditions

VUMC-DIPG-A, VUMC-DIPG-08, and VUMC-DIPG-10 were established at our institution. SU-DIPG-IV (20, 23), SU-DIPG-XIII (23), SU-DIPG-XXI, and SU-pcGBM-2 (20, 23) were established by Dr. Michelle Monje (Stanford University, Stanford, CA). HSJD-DIPG-07 (24), HSJD-DIPG-08, and HSJD-DIPG-12 cell lines were provided by Dr. Montero Carcaboso (Hospital San Joan de Déu Barcelona, Spain). The JHH-DIPG-01 (25) cell line was a gift from Dr. Raabe (Johns Hopkins Hospital, Baltimore, MD). The SF7761 and SF8628 (26) cell lines were generated by Dr. Hashizume (Northwestern University, Chicago, IL). VUMC-DIPG-A, VUMC-DIPG-08, SU-DIPG-XIII, HSJD-DIPG-07, HSJD-DIPG-08, SF7761, and SF8628 all possess the K27M mutation in *H3F3A*. SU-DIPG-IV and SU-DIPG-XXI harbor a K27M mutation in *HIST1H3B* instead, whereas VUMC-DIPG-10 and SU-pcGBM-2 did not have any mutations in genes encoding histone 3.

Neurospheres and adherent cell lines were cultured as described previously (27). All cell lines were routinely subjected to mycoplasma testing and only used for experiments when confirmed negative. Additionally, routine short tandem repeat (STR) analysis was performed using the Geneprint 10 system (Promega) to ensure cell line identity.

Murine DIPG cell lines

Mouse DIPG cell lines were derived from primary murine tumors generated by brainstem targeted in utero electroporation of piggyBac DNA plasmids, as described previously (28). Upon development of neurological symptoms, mice were sacrificed and cell lines were derived from pieces of primary tumors. Tumors were dissociated in papain (Worthington), and cultured as neurospheres as described.

Drugs and solutions

BGB324 was provided by BerGenBio, panobinostat, zosuquidar, elacridar, and AZD8055 were purchased from Axon Medchem. Apicidin and 4-iodo-SAHA were from Cayman Chemical. For *in vitro* studies, drugs were dissolved in DMSO at $>1,000\times$ the maximum used concentration. For animal studies, BGB324 was suspended in H₂O with 0.5% hydroxypropylmethylcellulose (Colorcon) and 0.1% Tween 80 (Sigma) and stirred overnight at 4°C on a magnetic stirrer before administration. For systemic administration, panobinostat was dissolved in 0.9% NaCl with 10% DMSO and 5% dextrose (formulation A) or 0.9% NaCl with 38% PEG, 3% dextrose, and 2% DMSO (formulation B). For convection-enhanced delivery (CED), panobinostat was dissolved in 0.9% NaCl containing 0.02% DMSO.

Lentiviral transductions

VUMC-DIPG-A and SF8628 were transduced with hTERT using the pLenti6-V5-hTERT-Blast plasmid, which was kindly provided by Professor Böcker of the Klinikum der Universität München, to ensure stable and continued growth. HSJD-DIPG-07 cells were lentivirally transduced using the pHIV-Luc-ZsGreen plasmid (Addgene, No. 39196). HSJD-DIPG-07, JHH-DIPG-01, and SU-DIPG-IV cells were lentivirally transduced using pLKO1-shAXL plasmids; shRNA sequences can be found in Supplementary Table S1.

Cell viability assays

Cell viability assays were performed in an identical way as described previously (27).

Migration and invasion assays

VUMC-DIPG-A and SF8628 cells were seeded in serum-containing medium at 10,000 cells/well in regular F-bottom 96-well plates. After 24 hours, a 300 $\mu\text{mol/L}$ wide scratch was made in all wells using a custom-made scratch tool. Afterwards, cells were washed once with PBS, fresh serum-containing medium was added and drugs were dispensed with a Tecan D300e Digital Dispenser at different concentrations. Cells were then incubated at 37°C in 5% CO₂ for 20 hours. Images were captured using a Leica DMI3000B optical microscope at $t = 0$ hours and $t = 20$ hours, after which scratch surface area was measured using Scratch Assay software (DCI Labs). Relative migration was defined as the relative decrease in scratch surface area compared with untreated controls.

Three-dimensional Matrigel invasion assays were performed as previously described, using growth factor-reduced Matrigel (Corning; ref. 29). Relative invasion was measured using ImageJ and defined as the relative radius of the invasive zone compared with the radius of the central neurosphere.

radiosensitization assays

On day 0, JHH-DIPG-01 and HSJD-DIPG-07 cells were seeded at 1,000 cells/well in 100 μ L serum-free medium in 96-well U-bottom plates with cell-repellent surfaces (Greiner Bio-One, No. 650970). The next day drugs were added using a Tecan D300e Digital Dispenser. Indicated plates were then subjected to 2 Gy radiation daily on day 1 to 5 using a Gammacell 220 Research Irradiator (MDS Nordion), accumulating to a total dose of 10 Gy. Starting day 6, medium was refreshed twice a week without addition of drugs. Regrowth of neurospheres was monitored by imaging spheres three times per week using a Leica DMI3000B optical microscope and measuring their size using ImageJ image analysis software (NIH). Monitoring continued until spheres reached their maximum size.

IHC and immunofluorescence

IHC and immunofluorescence (IF) were performed as described previously (30, 31). The following primary antibodies were used: Rabbit monoclonal anti-human AXL (IHC, 1:50, Clone C89E7; Cell Signaling technologies, No. 8661), goat polyclonal anti-human AXL (IF, 1:50; R&D Systems, AF154), goat polyclonal anti-mouse AXL (IHC, 1:50; R&D Systems, AF854), mouse monoclonal anti-human vimentin (IHC, 1:3,000, Clone V9; Thermo Fisher Scientific, No. MA5-11883), rabbit polyclonal anti-trimethyl-histone H3 (Lys27; IHC, 1:500; Millipore, No. 07-449) and rabbit polyclonal anti-H3K27M (IHC/IF, 1:500; Millipore, No. ABE419). Images were captured using a Zeiss Axio optical microscope equipped with a Zeiss Axiocam ICc 5 operated by ZEN Pro imaging software.

Western blot analysis

Cells were harvested during exponential growth for all Western blots, or after 24 hours exposure to drugs when stated, and snap frozen in liquid nitrogen. Frozen cell pellets were lysed for 60 minutes at 4°C with RIPA buffer [1% NP-40, 0.5% sodium deoxycholate, 0.1% SDS, 50 mmol/L Tris HCl pH 7.6, 150 mmol/L NaCl, 50 mmol/L β -glycerophosphate, 1 mmol/L DTT, 1x Complete Mini EDTA-Free Protease inhibitor Cocktail (Roche) and 1 mmol/L Na_3VO_4]. Primary antibodies used were rabbit polyclonal anti-SNAIL/SLUG (1:500; Abcam, No. 180714), rabbit polyclonal anti-ZEB1 (1:1,000; Sigma, No. HPA027524), rabbit polyclonal anti-ZEB2 (1:2,000; Sigma, No. SAB2102760), rabbit monoclonal anti-SOX2 (1:1,000; Abcam, No. 92494), rabbit monoclonal anti-Nestin (1:1,000; Abcam, No. 105389), rabbit monoclonal anti-human AXL tyrosine kinase (AXL) (1:1,000; Cell Signaling Technologies, No. 8661), goat polyclonal anti-mouse AXL (1:1,000; R&D Systems, No. AF854), rabbit polyclonal anti-phospho-AXL^{Y779} (1:1,000; R&D Systems, AF2228), rabbit monoclonal anti-FANCD2 (1:1,000; Abcam, No. a108928), mouse monoclonal anti-phospho-H2AX^{S139} (1:1,000; Millipore, No. 05-036), rabbit monoclonal anti-RAD51 (1:1,000; Cell Signaling Technologies, No. 8875), mouse monoclonal anti-TP53 (1:1,000; Thermo Scientific, No. MA5-12557), and mouse monoclonal anti-human Actin (1:5,000; Millipore, No. MAB1501). Western blotting procedure, antibody incubations, and readout were performed as described previously (27). Quantification of bands was performed using ImageJ.

Phospho-RTK arrays

Cells were harvested as described for Western blotting. Phospho-RTK antibody arrays (R&D Systems) were performed according to manufacturer's instructions, using 1 mg of protein per membrane. Chemiluminescent signals were captured on ECL Hyperfilm (Thermo Fisher Scientific, No. GX28906837) and films were developed using a

Kodak X-Omat 1000A developing system. Images were digitalized using a transmission-mode scanner.

RNA sequencing

Exponentially growing neurospheres from the JHH-DIPG-01, HSJD-DIPG-07, SU-DIPG-IV, and SF7761 cell lines were treated with 1 μ mol/L BGB324, 50 nmol/L Panobinostat, or the combination thereof for 24 hours prior to RNA extraction. RNA isolation, quality control, and sequencing procedure were performed as described previously (27). Fastq files were uploaded to the R2 platform (<http://r2.amc.nl>) for further analysis and statistics. Gene Ontology analysis was performed on all differentially expressed genes with an FDR-corrected *P* value <0.1. Parametric Analysis of Geneset Enrichment (PAGE) was performed using the KEGG pathways geneset collection, the 2015 Broad Institute GO terms and geneset collection. R2-generated heatmaps were ordered according to Spearman rank correlation coefficient. Reported *P* values are FDR-corrected and apply to pooled analyses of all four DIPG cultures under the same treatment condition.

In vivo studies

All animal experiments were performed in accordance with national and institutional guidelines and regulations and were approved by the Institutional Animal Care and Use Committees of the VU University Medical Center and The Netherlands Cancer Institute. Supportive care, such as perioperative pain relief and easy access to food and water, was provided as indicated by these guidelines.

For efficacy studies, female athymic nude mice (Balb/c outbred; Envigo) were intracranially injected with 500,000 HSJD-DIPG-07-Fluc or UC-8D2 cells. Injection procedure, follow-up by bioluminescence imaging (BLI) and MRI were performed as described previously (27). In therapeutic experiments using HSJD-DIPG-07-Fluc and UC-8D2, treatment was started 2 and 1 week(s) after injection of tumor cells, respectively, upon demonstration of engraftment by BLI. Mice were stratified among treatment groups based on signal intensity on BLI. In the first experiment using HSJD-DIPG-07-Fluc xenografts, mice received vehicle, 150 mg/kg/day of BGB324 via oral gavage and/or 10 mg/kg/day panobinostat (formulation A) via intraperitoneal injection for 4 days. In the second experiment using HSJD-DIPG-07-Fluc xenografts, mice received vehicle or 150 mg/kg/day BGB324 for 2 weeks. In addition, half of the mice received panobinostat via CED (2 μ mol/L, 15 μ L in 30 minutes) on day 3 of treatment. In the experiment using UC-8D2 allografts, mice received vehicle or 150 mg/kg/day BGB324 via oral gavage for 2 weeks, panobinostat 10 mg/kg/day (formulation B) via intraperitoneal injection on days 1 to 5 and days 11 to 13, or the combination thereof. Mice were inspected daily and sacrificed upon display of severe neurological symptoms (eg, limb weakness, incoorrectable head tilt, ataxia, convulsions) or upon losing >20% body weight.

In vitro drug transporters assays and in vivo BBB penetration of BGB324

In vitro drug transporter assays were performed as described previously (27). For BBB penetration studies of BGB324 WT, Bcrp1^{-/-}, Mdr1a/b^{-/-}, and Bcrp1;Mdr1a/b^{-/-} FVB mice were used. BGB324 was administered intravenously at a dose of 10 mg/kg in a formulation consisting of DMSO:Cremophor EL:saline (1:1:8). Blood was collected 1 hour after administration by cardiac puncture under isoflurane anesthesia, and brains were subsequently collected. As a result of this order of action, the blood pool in the brain of the mouse has a negligible influence on the determination of BGB concentrations.

Further preparation of tissue and blood samples and LC/MS-MS analysis of drug concentrations was performed as described previously (27). The only modification concerned the multiple reaction monitoring, which was performed at 507.6/436.5 (BGB234), 350.4/158.2 (panobinostat), and 418.2/138.4 (AZD8055).

Statistical analysis

In vitro dose–response curves were fitted with the log(inhibitor) versus response–variable slope (four parameters) curve to determine IC_{50} s. Survival percentages in synergy experiments were statistically compared using the unpaired two-sided Student *t* test. Drug synergy was calculated using the combination index (CI) formula as described by Chou and Talaly, which compares the expected effect of the combination of any two drugs with the observed effect (32). Any value over 1 implies antagonism, whereas values below 1 are indicative of synergistic effects. We considered any value below 0.5 as a measure of strong synergy.

Growth curves of neurospheres in the radiosensitization assays were compared by multilevel regression analysis of log-transformed relative sphere sizes. Both differences in growth between groups and interactions between determinants (drugs and/or radiation) were evaluated this way. Resulting regression coefficients were retransformed and used to determine relative growth speeds of neurospheres. These values were used as input values for the CI formula as described by Chou and Talaly (32).

Statistical analysis of pharmacokinetic and drug transporter experiments was done as described previously (27). Bioluminescence data on day 8 were analyzed using Microsoft Excel, using the independent *t* test to compare treatment groups. Longitudinal bioluminescence data were compared by multilevel regression analysis as described above for the radiosensitization assays. Kaplan–Meier curves were generated and compared using the log-rank (Mantel–Cox) test. The statistical analyses were performed with Excel, Graphpad Prism (version 6), and SPSS (version 22), and a *P* value <0.05 was considered statistically significant. All tests were performed two-sided unless otherwise stated. Outliers were not excluded in any of the experiments, with the exception of one mouse in the UC-8D2 therapeutic trial with an aberrant growth pattern on BLI; this did not influence study results.

Results

The RTK AXL is activated in DIPG

Analysis of published data from a recent study (33) shows that introduction of H3K27M in murine embryonic hindbrain neural stem cells (NSC) induces a mesenchymal gene expression pattern in these cells (Supplementary Fig. S1), explaining the mesenchymal transition previously observed in DIPG (3, 5). To identify potential targetable drivers of the mesenchymal transition in these tumors, we analyzed a publicly available dataset of gene expression profiles of biopsy samples from patients with DIPG for expression of kinases known to be involved in this process (34). This revealed high mRNA expression of the RTK AXL, which has previously been described as an initiator of the mesenchymal transition in adult GBM (14–18). The average expression of AXL in DIPG ($n = 37$) was twofold higher than in normal brain (35) and cerebellar (36) tissue (Fig. 1A). The related TAM-RTK subfamily members *MERTK* and *TYRO3* were less evidently overexpressed (*MERTK*) or even repressed (*TYRO3*) in DIPG samples compared with normal brain and cerebellar tissue (Fig. 1A). Moreover, gene set enrichment analysis (GSEA) of this dataset revealed a high correlation between AXL expression in DIPG and

the mesenchymal gene expression signature in GBM (FDR $P < 0.05$, Fig. 1B; ref. 37). Furthermore, knockdown of H3.3K27M has been shown to decrease the expression of AXL in DIPG cells (38). To demonstrate that mRNA overexpression of AXL in these samples was due to AXL expression by tumor cells, we performed IF staining of a diagnostic specimen of a H3.3 K27M-positive DIPG tumor biopsy. This revealed high expression levels of AXL in tumor cells, which were identified by costaining with a H3K27M-specific antibody (Fig. 1C). Furthermore, staining of AXL and H3K27M was confirmed by IHC in a H3.1K27M mutated DIPG autopsy specimen (Supplementary Fig. S2A), and by IF in HSJD-DIPG-07 patient-derived xenografts (Supplementary Fig. S2B), whereas healthy human pontine tissue revealed only background staining of both proteins (Supplementary Fig. S2C), in line with previously published data (39). In addition, immunoblotting using phospho-RTK arrays revealed moderate to high levels of phosphorylated AXL protein, and low to absent *MERTK* and *TYRO3* phosphorylation, in all patient-derived cell cultures tested (Fig. 1D; Supplementary Fig. S3A), thereby validating primary DIPG neurospheres as a model to study the role of AXL in DIPG biology. The presence of AXL and its phosphorylation at Y779 was further confirmed by Western blotting in all DIPG cultures used in this study (Fig. 1E). Finally, these findings were further confirmed using a murine DIPG model (UC-8D2; ref. 28), in which tumor growth was induced by intra-uterine electroporation of mouse embryos on day E13, of constructs expressing *Pdgfra*^{D842V}, dominant negative Trp53 (DNp53), and *H3f3a*^{K27M}. This murine DIPG model was validated by IHC, which showed diffusely growing tumors with cells staining positive for AXL, H3K27M mutant protein and negative for H3K27 trimethylation (Supplementary Fig. S2D).

The AXL inhibitor BGB324 synergizes with panobinostat to decrease DIPG cell viability and migration

On the basis of the identification of AXL in patients specimens and its activation in DIPG neurosphere cultures, we investigated the potential antitumor effect of AXL inhibition. Therefore, we treated primary DIPG neurospheres for 96 hours with varying concentrations of the specific AXL inhibitor BGB324 (Fig. 2A; ref. 19). Viability of DIPG neurospheres decreased at micromolar concentrations, with the notable exception of the *HIST1H3B* mutant cell line SU-DIPG-XXI, which had an IC_{50} of less than 500 nmol/L. No difference in viability was observed between H3K27M and H3WT DIPG cells treated with BGB324. As antibodies to the primary site of action of BGB324 (p-AXL^{Y821}; ref. 19) are unavailable, the on-target effect of BGB324 was demonstrated by showing a decrease in the secondary target site p-AXL^{Y779} in JHH-DIPG-01, SU-DIPG-IV, HSJD-DIPG-07, VUMC-DIPG-A, and SF8628 cells, upon exposure to 1 μ mol/L BGB324 for 24 hours (Supplementary Fig. S3B). To determine the effect of BGB324 treatment on gene expression, we then performed RNA sequencing (RNA-seq) on four primary DIPG cultures after 24 hours treatment with BGB324. In line with previous publications, a significant negative geneset enrichment of mesenchymal gene expression profiles, as well as a concurrent enrichment in expression of an epithelial differentiation geneset, was observed after treatment (Fig. 2B). Consistent with the association between the mesenchymal phenotype and invasive behavior of cancer cells, shRNA-mediated knockdown of AXL almost completely abrogated the capacity of HSJD-DIPG-07 neurospheres for invasion in a 3D matrigel assay. Concordantly, a strong and dose-dependent inhibition of invasion was seen in JHH-DIPG-01 and SF7761 neurospheres upon treatment with BGB324 (Fig. 2C).

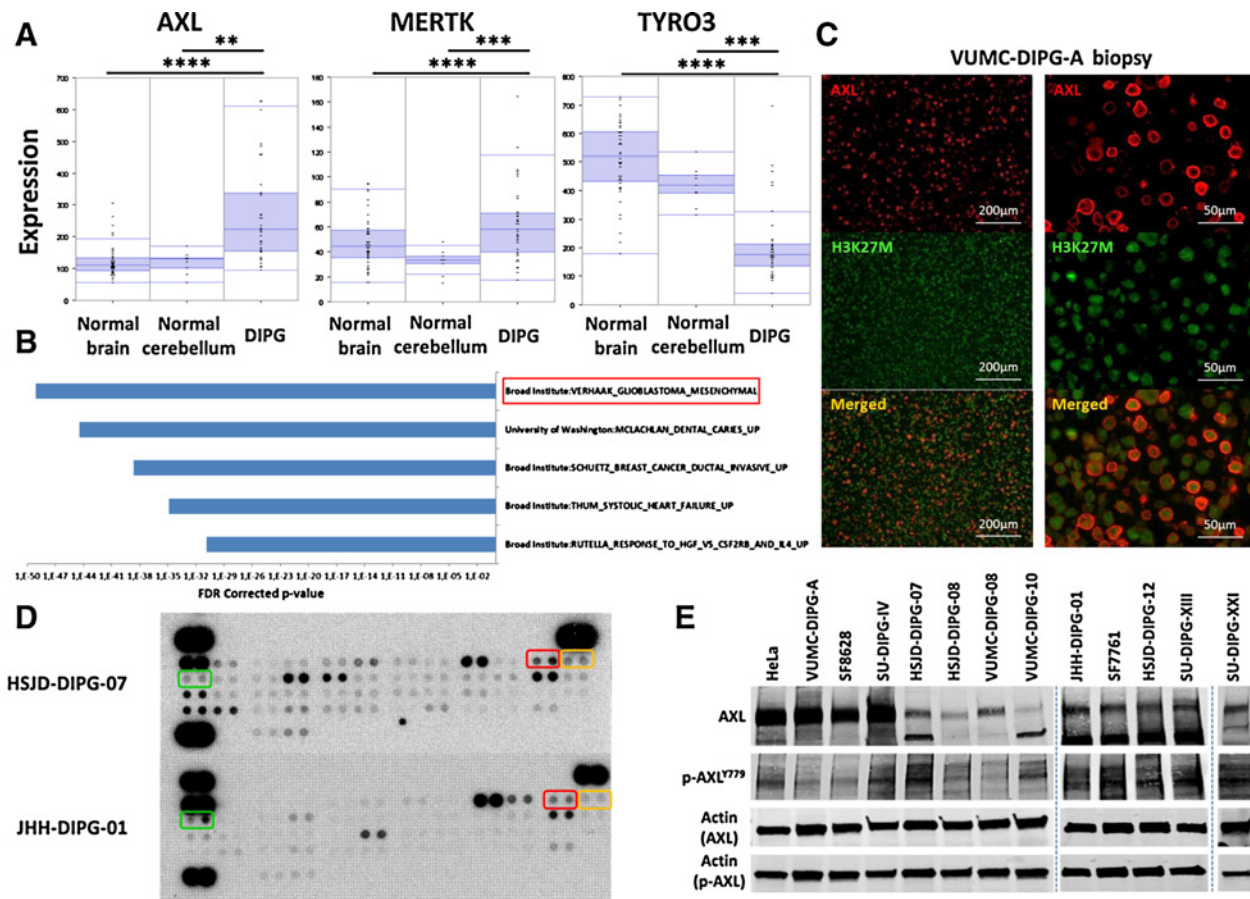


Figure 1. Expression of AXL, MERTK, and TYRO3 in DIPG. **A**, mRNA expression levels of *AXL*, *MERTK*, and *TYRO3* in normal brain, cerebellum, and DIPG patient samples ($n = 37$; GSE 13564, 3526, and 26576; refs. 34–36; **, $P < 0.01$; ***, $P < 0.001$; ****, $P < 0.0001$ (two-sided independent t test). **B**, PAGE of genes with expression positively correlated to *AXL* expression (FDR $P < 0.05$) in a publicly available gene expression dataset of DIPG patient samples (GSE 26576; ref. 34). Top five most significantly enriched genesets are shown. **C**, IF staining for AXL in tumor tissue from patient VUMC-DIPG-A, obtained by needle biopsy. Costaining of AXL and H3K27M shows high expression of AXL (red) in tumor cells, as identified by H3K27M expression (green; see also Supplementary Fig. S2). **D**, Phospho-RTK array showing AXL phosphorylation in DIPG neurospheres (two of six cell lines shown, see also Supplementary Fig. S3). Colored boxes indicate locations of AXL (red), MERTK (yellow), and TYRO3 (green) on the array. **E**, Composite Western blot analysis showing AXL and p-AXL^{Y779} expression in 12 primary DIPG cultures used in this study. Separate gels are indicated by the blue dotted lines. HeLa cells were used as a positive control, actin was used as a loading control.

Given that reversal of the mesenchymal transition by inhibition of AXL sensitizes tumor cells in other types of cancer, including GBM, to cytotoxic therapies, we set out to develop a combination treatment strategy for DIPG (14–19). For this purpose, we chose the histone deacetylase (HDAC) inhibitor panobinostat for its proven preclinical efficacy in DIPG and its capacity to inhibit the mesenchymal phenotype of cancer cells in its own right via different molecular pathways (20–22). Sensitivity of DIPG neurospheres to treatment with panobinostat monotherapy was in line with previous publications, with IC₅₀ concentrations between 10 and 100 nmol/L (Fig. 3A; refs. 20, 40). Combined treatment of DIPG neurospheres with 1 μmol/L BGB324 and 10 to 100 nmol/L panobinostat revealed a strong synergistic decrease in cell viability in seven of nine DIPG cell lines tested. Combination indices (CI), calculated according to Chou and Talaly (32), ranged from 0.04 to 0.98, with most H3K27M mutant DIPG cultures displaying CIs below 0.5 (Fig. 3B and C; Supplementary Fig. S4). In contrast, this combined treatment had no synergistic effect on histone 3 wild-type (WT) pediatric GBM cells (SU-pcGBM2) and even a protective effect on the viability of H3 WT VUMC-DIPG-10

cells, implying selective sensitivity of cells harboring an H3K27M mutation. This selective synergistic effect of BGB324/panobinostat on H3K27M cells was further confirmed in neurospheres derived from the two murine DIPG models, expressing either H3f3a^{K27M} (UC-8D2) or WT H3f3a (UC-4B2; Supplementary Fig. S5A). Expression of AXL and p-AXL^{Y779} in these cells was confirmed by Western blotting (Supplementary Fig. S5B). Treatment of DIPG cells with BGB324 and two other HDAC inhibitors, apicidin and 4-iodo-SAHA, resulted in a synergistic, although weaker, antiproliferative effect as well, demonstrating that this synergy is not related to off-target effects of panobinostat (Supplementary Fig. S4C). Conversely, shRNA-mediated knockdown of AXL in HSD-DIPG-07, JHH-DIPG-01, and SU-DIPG-IV cells strongly sensitized these cells to treatment with panobinostat, confirming that the observed synergy between BGB324 and HDACi is dependent on AXL (Supplementary Fig. S6). Finally, combined treatment with BGB324 and panobinostat of adherent monolayers of two H3K27M DIPG cell lines, VUMC-DIPG-A and SF8628, additively reduced migration of DIPG cells in a scratch assay (Fig. 3D and E).

Downloaded from <http://aacrjournals.org/clinccancerres/article-pdf/26/13/3319/2061063/3319.pdf> by guest on 24 December 2022

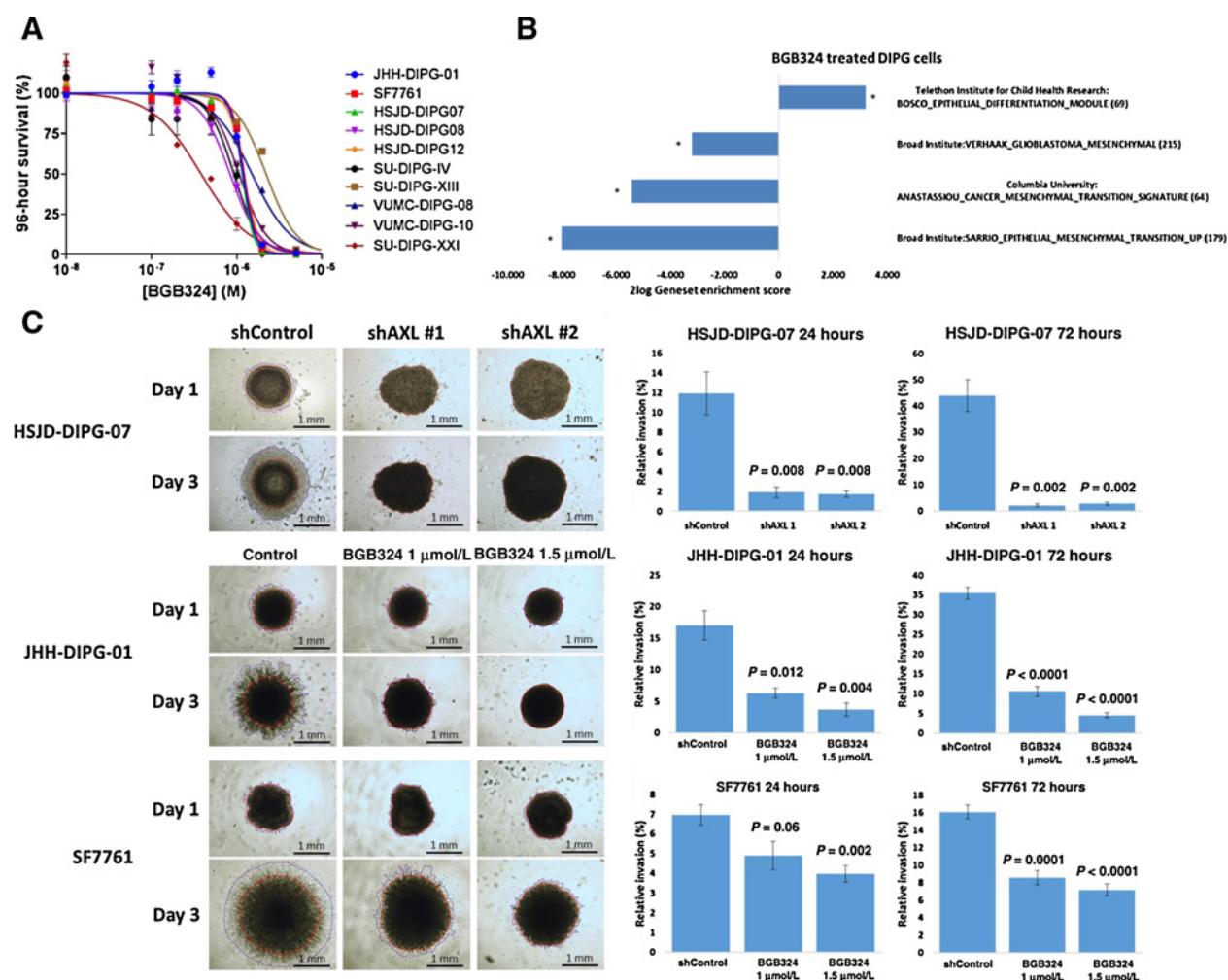


Figure 2.

Effects of AXL inhibition in DIPG cultures. **A**, Dose–response curve showing viability of primary DIPG cells after 96 hours exposure to BGB324. Results are shown as relative fitted survival \pm SEM ($n = 5$). **B**, PAGE of genesets associated with the mesenchymal transition in four primary DIPG cell lines (JHH-DIPG-01, HSJD-DIPG-07, SF7761, SU-DIPG-IV) after treatment with 1 μ mol/L BGB324 for 24 hours (*, FDR-corrected $P < 0.05$). **C**, 3D Matrigel invasion assay showing abrogated invasion of HSJD-DIPG-07 cells upon shRNA-mediated AXL knockdown and of JHH-DIPG-01 and SF7761 cells upon treatment with BGB324, 24 and 72 hours after immersion of neurospheres in Matrigel. Red line demarcates central neurosphere, purple line invasive zone. Quantification is presented as relative invasion (%) \pm SEM ($n = 6$) and tested for significance by independent two-sided t test.

Combined AXL and HDAC inhibition reverses the mesenchymal transition in DIPG cells

Because both BGB324 and panobinostat have been shown to down-regulate the expression of mesenchymal genes and proteins in different types of cancer (18, 19, 21, 22), we studied the effects of these drugs on the expression of master transcriptional regulators of mesenchymal transition in DIPG cultures. Therefore, JHH-DIPG-01, SF7761, and SU-DIPG-IV neurospheres were exposed for 24 hours to panobinostat and/or BGB324 before lysing the cells for protein analyses. Western blotting revealed a decrease in levels of the master regulators of the mesenchymal transition SNAIL/SLUG, ZEB1, and a modest decrease of ZEB2 (Fig. 4A), which was mainly caused by panobinostat but enhanced by addition of BGB324. In line with the published connection between the mesenchymal and stem cell phenotype of cancer cells (8–13), we also detected a downregulation of stem cell markers SOX2 and Nestin in DIPG cells after treatment with panobinostat and BGB324 (Fig. 4A). Subsequently, neurospheres from four different

patient-derived DIPG cell cultures (JHH-DIPG-01, SF7761, HSJD-DIPG-07, and SU-DIPG-IV) were treated with panobinostat and/or BGB324 for 24 hours to study gene expression. In line with the result from Western blotting, RNA-seq of these samples revealed a down-regulation of *SNAI2*, *ZEB1* and *ZEB2*, *CDH2*, *SOX2*, and *NES*, upon treatment with panobinostat, which was further enhanced in cells treated with a combination of panobinostat and BGB324 (Fig. 4B). Analysis of a set of genes known to be involved in initiation and maintenance of the mesenchymal transition (4), demonstrated down-regulation of the vast majority of these genes, which was most pronounced in the samples treated with both panobinostat and BGB324 (Fig. 4C).

Besides genes involved in the mesenchymal transition, a general downregulation of SOX2 target genes, as defined by Ben-Porath and colleagues (41), was identified in our RNA-seq dataset (Fig. 4D). Correspondingly, a gene expression signature associated with neuronal differentiation (42) was observed in DIPG cells treated with

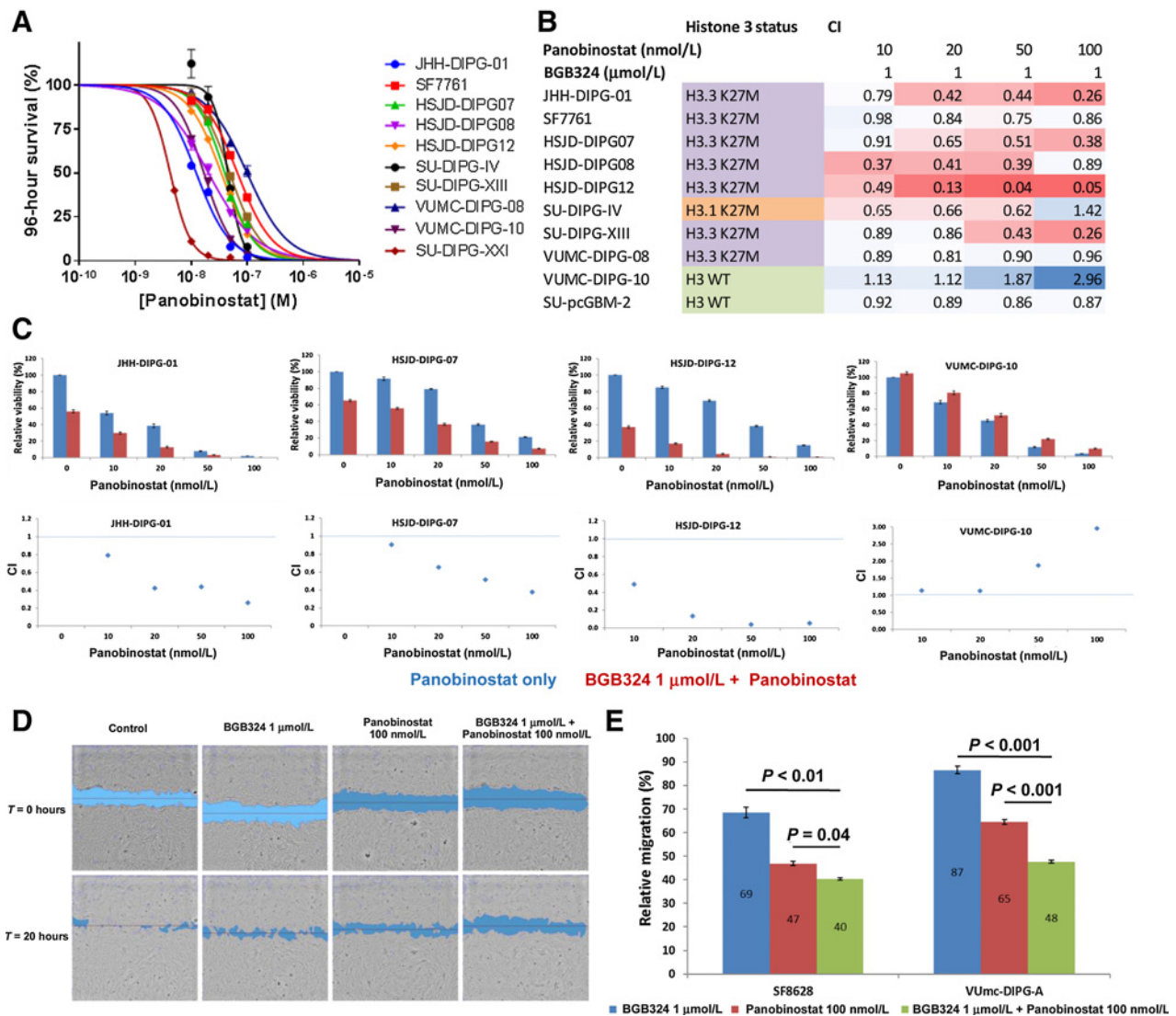


Figure 3. Synergistic antitumor effect of BGB324 and panobinostat on H3K27M DIPG cells. **A**, Dose-response curves of DIPG neurospheres treated for 96 hours with varying concentrations of panobinostat. Results are shown as relative survival \pm SEM ($n = 5$). **B**, CIs (32) of relative viability of primary DIPG cell lines exposed for 96 hours to 1 μ mol/L BGB324 and varying concentrations of panobinostat. SU-DIPG-XXI is not represented as synergy occurred in a different concentrations range (Supplementary Fig. S4). **C**, Top: Relative survival of primary DIPG cultures treated with 1 μ mol/L BGB324 and varying concentrations of panobinostat (red) or panobinostat monotherapy (blue). Results are shown as average survival (%) \pm SEM ($n = 5$). Bottom: corresponding CIs of combination treatment of DIPG cultures with BGB324 and panobinostat at varying concentrations. Four representative examples are shown, see also Supplementary Figs. S4–S6. **D**, Scratch assay measuring migration of VUMC-DIPG-A cells treated with 1 μ mol/L BGB324, panobinostat 100 nmol/L, or the combination thereof over a period of 20 hours. **E**, Relative 20-hour migration, defined as the reduction in scratch area after 20 hours compared with untreated controls, of VUMC-DIPG-A and SF8628 cells treated with 1 μ mol/L BGB324, panobinostat 100 nmol/L, or the combination thereof. Data are presented as average relative migration \pm SEM ($n = 5$) and compared by independent *t* test.

BGB324 and panobinostat (Fig. 4E). PAGE showed that five of the ten most significantly enriched Gene Ontology (GO) terms after treatment with BGB324 and panobinostat directly involved synapse functioning, with the remaining five GO terms being indirectly associated with nerve cell function (Fig. 4F). These results are in slight contrast with the enrichment in epithelial gene expression patterns seen after treatment with BGB324 alone (Fig. 2B), which is likely a consequence of the interaction of BGB324 and panobinostat on a transcriptional level. Together, these results imply that with

combination treatment of DIPG cells with BGB324 and panobinostat the gene expression profile shifts from a mesenchymal, stem cell-like, to a neural pattern.

Combined treatment with BGB324 and panobinostat synergistically sensitizes DIPG cells to radiation

Given the importance of radiotherapy in the treatment of DIPG, and the reported connection between mesenchymal transition and therapy response of tumors (6–9, 43), we sought to determine whether

Downloaded from <http://aacrjournals.org/clinccancerres/article-pdf/26/13/3319/2061063/3319.pdf> by guest on 24 December 2022

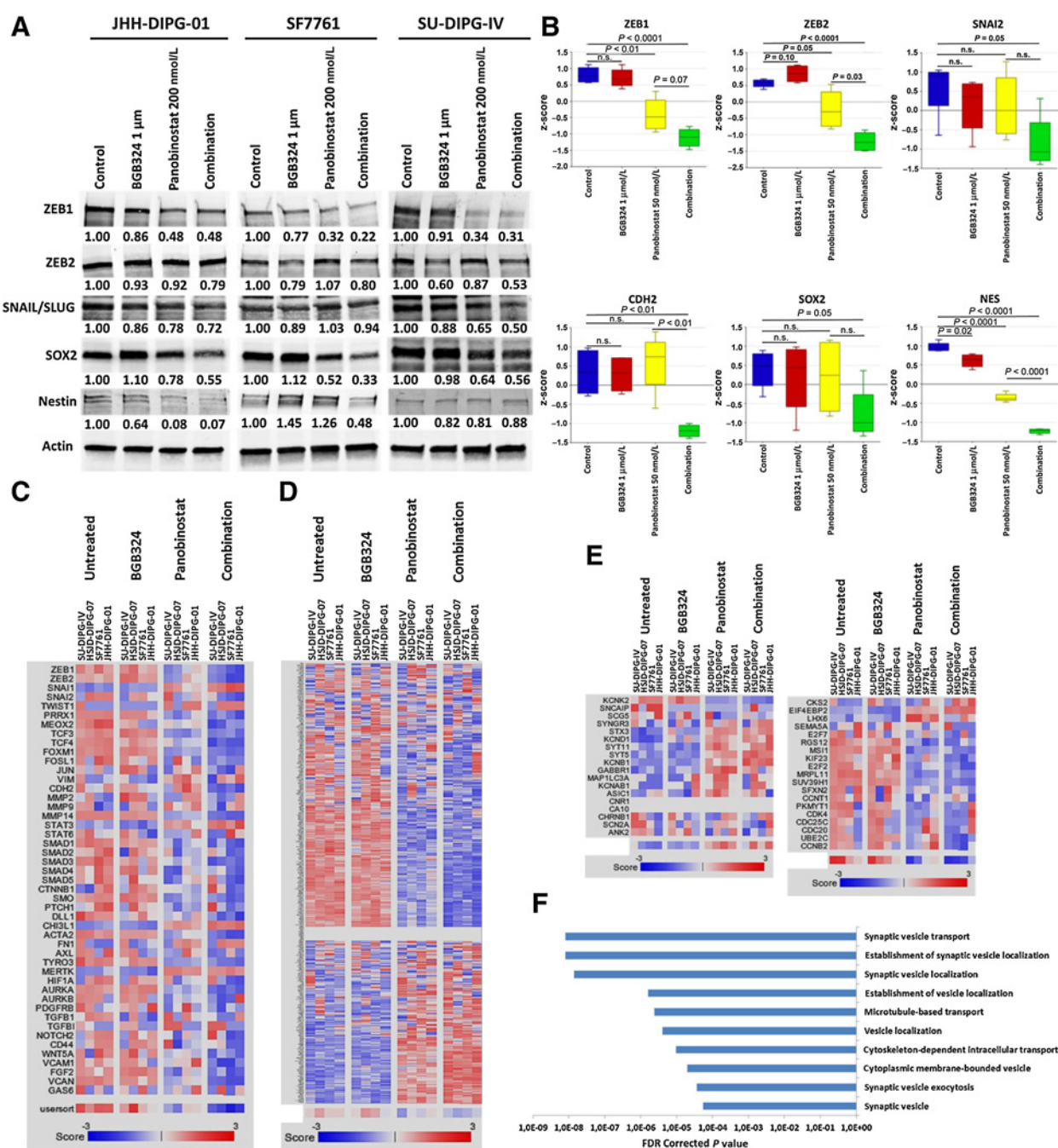


Figure 4. Reversal of the mesenchymal and stem-like phenotype of DIPG cells by BGB324 and panobinostat. **A**, Representative Western blots (≥ 2 biological replicates) showing expression of ZEB1, ZEB2, SNAIL/SLUG, SOX2, and Nestin after 24 hours treatment of JHH-DIPG-01, SF7761, and SU-DIPG-IV neurospheres with 1 $\mu\text{mol/L}$ BGB324, 200 nmol/L panobinostat, or the combination thereof. Actin was used as a loading control and to correct quantification, one representative actin is shown. **B**, Box plots showing RNA expression (z score) of ZEB1, ZEB2, SNAI2, CDH2, SOX2, and NES in four primary DIPG cell lines (SU-DIPG-IV, HSJD-DIPG-07, SF7761, and JHH-DIPG-01) after 24 hours treatment with 1 $\mu\text{mol/L}$ BGB324, 50 nmol/L panobinostat, or the combination thereof. P values were calculated by independent two-sided t test. **C**, Heatmap showing expression (z score) of mesenchymal transition-associated genes (4) in the same samples. **D**, Heatmap showing expression (z score) of SOX2 target genes (41). **E**, Heatmap showing expression (z score) of genes upregulated (left) and downregulated (right) in neuronal differentiation (42). **F**, GO analysis of genes upregulated after treatment of the four cell lines from c with both 1 $\mu\text{mol/L}$ BGB324 and 50 nmol/L panobinostat for 24 hours. Top 10 GO terms based on significance are shown. *, FDR P value < 0.01 .

Downloaded from <http://aacrjournals.org/clinccancerres/article-pdf/26/13/3319/2061063/3319.pdf> by guest on 24 December 2022

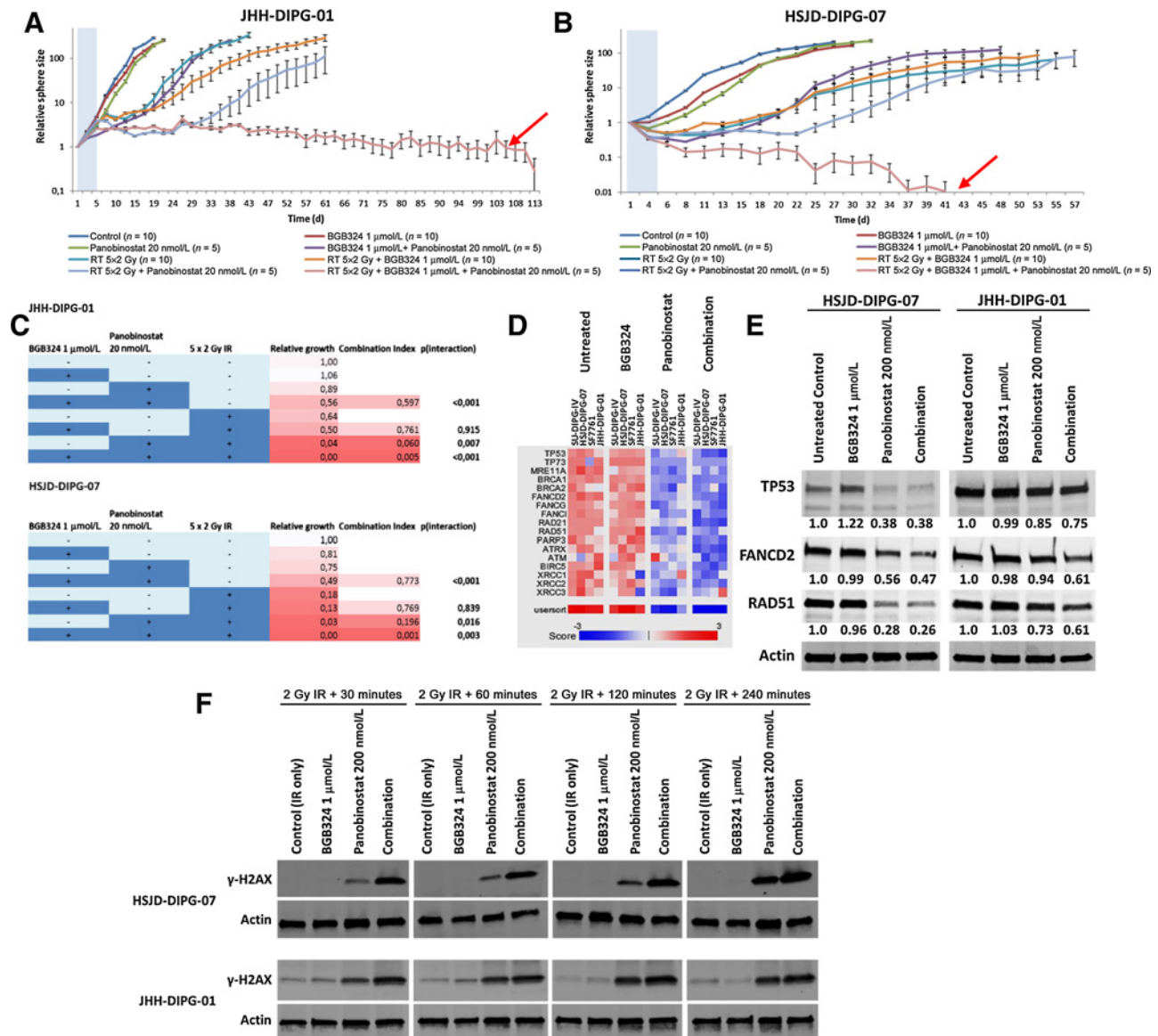


Figure 5. Synergistic radiosensitization of DIPG neurospheres by BGB324 and panobinostat. **A** and **B**, Long-term culture of p53^{mut} JHH-DIPG-01 (**A**) and p53^{WT} HSJD-DIPG-07 (**B**) neurospheres treated with 1 μmol/L BGB324, 20 nmol/L panobinostat, 5 × 2 Gy IR, or any combination thereof from day 1 to 5 (blue fields). Values represent average relative sphere size (fold change) ± SEM. Blue area indicates treatment period, after which spheres were allowed to regrow under optimal conditions. Red arrows indicate growth curves of DIPG neurospheres exposed to triple therapy. Five to ten technical replicates are shown per condition. **C**, Relative growth speed, CI, and *P* values of interactions, derived from multilevel regression analysis of curves in (**A** and **B**). **D**, Expression (*z* score) of genes associated with IR-induced DNA damage repair in the same samples. **E**, Representative Western blot analysis showing levels of *TP53*, *FANCD2*, *RAD51* in JHH-DIPG-01 and HSJD-DIPG-07 cells after 24 hours treatment with 1 μmol/L BGB324, 200 nmol/L panobinostat, or the combination thereof. Actin was used as a loading control and to correct quantification. See also Supplementary Fig. S7, which shows the same experiment in cells receiving an additional 2 Gy IR. **F**, Representative Western blot analysis showing levels of γ-H2AX in JHH-DIPG-01 and HSJD-DIPG-07 cells treated as in (**E**), with the addition of 2 Gy IR 30, 60, 120, and 240 minutes before sample collection. Control cells received only 2 Gy IR without drug treatment. Actin was used as a loading control.

treatment with BGB324 and/or panobinostat could sensitize DIPG neurospheres to ionizing radiation (IR). Therefore, p53^{mut} JHH-DIPG-01 and p53^{WT} HSJD-DIPG-07 neurospheres were exposed to 1 μmol/L BGB324, 20 nmol/L panobinostat, a clinically relevant dose of 10 Gy fractionated IR (2 Gy daily) or any combination thereof. After 5 days, all treatment was withdrawn and regrowth of neurospheres was monitored until maximum sphere size was reached. Panobinostat significantly and strongly sensitized DIPG cells to IR, although

regrowth of the neurospheres was eventually observed (JHH-DIPG-01: *P* = 0.007; CI = 0.060 and HSJD-DIPG-07: *P* = 0.016; CI = 0.196; **Fig. 5A–C**). Addition of BGB324, having no significant radiosensitizing effect on its own, produced robust triple synergy in combination with panobinostat and fractionated irradiation (JHH-DIPG-01: *P* < 0.001; CI = 0.005 and HSJD-DIPG-07: *P* = 0.003; CI = 0.001; **Fig. 5A–C**) and completely abolished neurosphere regrowth in our assay, even after >3 months of follow-up measurements.

To explain the radiosensitizing capacity of panobinostat, and the enhancement thereof by BGB324, we analyzed expression of genes involved in DNA repair in our RNA-seq datasets, which revealed a downregulation of genes known to be essential to IR-induced DNA damage repair. Again, the strongest downregulation was generally seen in DIPG cells treated with both BGB324 and panobinostat (Fig. 5D). Western blotting of HSJD-DIPG-07 and JHH-DIPG-01 cells treated for 24 hours with BGB324 and/or panobinostat confirmed the downregulation of TP53, FANCD2, and RAD51, which was strongest in cells treated with both agents (Fig. 5E), with downregulation of TP53 being more pronounced in p53^{WT} HSJD-DIPG-07 than in p53^{mut} JHH-DIPG-01 cells. No difference in downregulation of these proteins was seen upon simultaneous exposure of DIPG cells to 2 Gy IR (Supplementary Fig. S7). Consequently, an accumulation of γ -H2AX was seen after 2 Gy IR in DIPG cells treated for 24 hours with BGB324 and/or panobinostat, which occurred earlier and was more prominent in those cells receiving combination treatment (Fig. 5F).

BGB324 crosses the BBB

One of the most important reasons for therapy failure in DIPG is thought to be the presence of an intact BBB. To assess the potential clinical applicability of BGB324 for the treatment of DIPG, we investigated its potential to cross the BBB. We first determined the affinity of the multidrug transporters MDR1 and BCRP, which are highly active on the BBB, for BGB324 and panobinostat. For this, we used previously described concentration equilibrium transport assays (44), in which the apical-to-basal and basal-to-apical transport across a monolayer of BCRP/Bcrp1 and MDR1/Mdr1a expressing cells is measured. Assays were performed in the presence of zosuquidar (MDR1 inhibitor) and/or elacridar (MDR1/BCRP inhibitor) to demonstrate the specificity of the observed influence of overexpression of the respective multidrug transporters. These assays revealed panobinostat as a substrate for both MDR1 and BCRP with roughly equal affinity (Supplementary Fig. S8), even though it has been reported to reach therapeutic concentrations in mouse brain after systemic administration (20). BGB324 proved to be a substrate for MDR1 and murine Bcrp1, but not human BCRP *in vitro* (Supplementary Fig. S9A). To determine if this would limit therapeutic prospects, we administered 10 mg/kg BGB324 intravenously to WT mice, or mice lacking the drug efflux transporters Mdr1a/b and/or Bcrp1 (Mdr1a/b^{-/-}, Bcrp1^{-/-}, and Mdr1a/b^{-/-};Bcrp1^{-/-}), 1 hour before sacrificing them to collect blood and brain tissue. Mass spectrometric analysis of the BGB324 concentration in brain and plasma revealed no significant differences in plasma concentration between the different genotypes of mice, but different brain:plasma ratios. WT mice had a brain:plasma ratio of 0.44 (95% CI, 0.28–60), compared with 3.78 ($P < 0.0001$; 95% CI, 3.60–3.96) for Mdr1a/b^{-/-} mice, 0.33 ($P = \text{n.s.}$; 95% CI, 0.27–0.40) for Bcrp1^{-/-} mice, and 3.59 ($P < 0.01$; 95% CI, 2.62–4.55) for Mdr1a/b^{-/-};Bcrp1^{-/-} mice (Supplementary Fig. S9B). Although this indicates that BGB324 is a substrate of MDR1 and—to a lesser extent—BCRP, these values correspond with an absolute brain concentration of nearly 1,200 pmol/g (~1.2 $\mu\text{mol/L}$) BGB324 in WT mice at 1 hour after administration of a low dose of BGB324. On the basis of the *in vitro* results this would be sufficient to achieve an antitumor effect in the brain.

Combined treatment with BGB324 and panobinostat prolongs survival of mice with DIPG xenografts

To further investigate the clinical potential of the combination of BGB324 and panobinostat for the treatment of DIPG, we tested these

drugs in a therapeutic study using mice bearing HSJD-DIPG-07-Fluc orthotopic xenografts. To assure that this xenograft model was representative of the human disease, MRI was performed 6 weeks after injection. This showed no contrast enhancement of the tumor-bearing pontine region after administration of gadolinium, recapitulating the intact BBB seen in patients (Fig. 6A). Moreover, IHC and IF confirmed a diffuse growth pattern and expression of AXL in these tumors (Fig. 6B; Supplementary Fig. S2B), as observed in primary patient material.

To test the therapeutic potential of the combination of BGB324 and panobinostat, treatment was initiated upon demonstration of engraftment of HSJD-DIPG-07-Fluc cells by BLI 2 weeks after pontine injection of tumor cells. Mice received either vehicle, BGB324 150 mg/kg/day, panobinostat 10 mg/kg/day in formulation A for 4 days or the combination thereof. Eight days after initiation of therapy, BLI indicated a significant delay in tumor growth in the mice receiving both BGB324 and panobinostat (tumor growth inhibition $77 \pm 16\%$, $P < 0.05$; Fig. 6C). Although no toxicity was observed after treatment with BGB324 alone, this regimen of systemic administration of panobinostat was poorly tolerated by the animals. Therefore, a subsequent experiment was performed in which panobinostat was administered via CED. Mice received either vehicle or 150 mg/kg/day BGB324 for 2 weeks, starting 2 weeks after injection of tumor cells. In half the mice from both groups, this was followed by a single CED treatment consisting of 15 μL of 2 $\mu\text{mol/L}$ panobinostat (20) on day 3 of the treatment with BGB324. This treatment schedule was well tolerated and resulted in a modest increase in median survival from 45 to 61 days after start of treatment ($P < 0.01$ for all comparisons, log-rank test) in the group receiving both BGB324 and panobinostat, whereas either treatment alone did not significantly increase survival of the mice (Fig. 6D). To validate these results in a second DIPG model, we treated mice bearing UC-8D2 murine DIPG orthotopic allografts with BGB324 150 mg/kg/day for 14 days, panobinostat 10 mg/kg/day in formulation B for 5 days or the combination thereof. Mice receiving panobinostat received a second course of 3 days at the same dose after an interval of 5 days. This formulation of panobinostat was better tolerated by the mice, and no added toxicity of combined treatment with BGB324 was seen in this trial. After 8 days of treatment, BLI of the hindbrain demonstrated a significant decrease in tumor size in mice treated with BGB324 and panobinostat ($P = 0.02$, Fig. 6E). Three mice receiving combination therapy achieved an objective response, defined as a reduction of >50% in BLI signal, compared with none in the other treatment arms (χ^2 test for trend, $P = 0.019$). Longitudinal follow-up of tumor size by BLI for a period of 4 weeks revealed a significant delay in tumor growth in mice receiving both BGB324 and panobinostat, compared with mice receiving vehicle or monotherapy ($P < 0.05$ for all comparisons, Fig. 6F). Correspondingly, treatment of mice bearing UC-8D2 allografts with BGB324 and panobinostat resulted in a modest, yet significant increase in median survival of 12 days for the combination treatment arm only ($P = 0.02$, log-rank test, Fig. 6G).

Discussion

Despite major advances in the understanding of the biology of DIPG in the past decade, an effective therapy is still not available. In 2015, the international preclinical DIPG consortium identified panobinostat as a promising novel therapeutic agent with antitumor efficacy in preclinical DIPG models (20). However, this same consortium showed that DIPG cell cultures and xenografts rapidly developed resistance to panobinostat, necessitating the search for additional antitumor agents

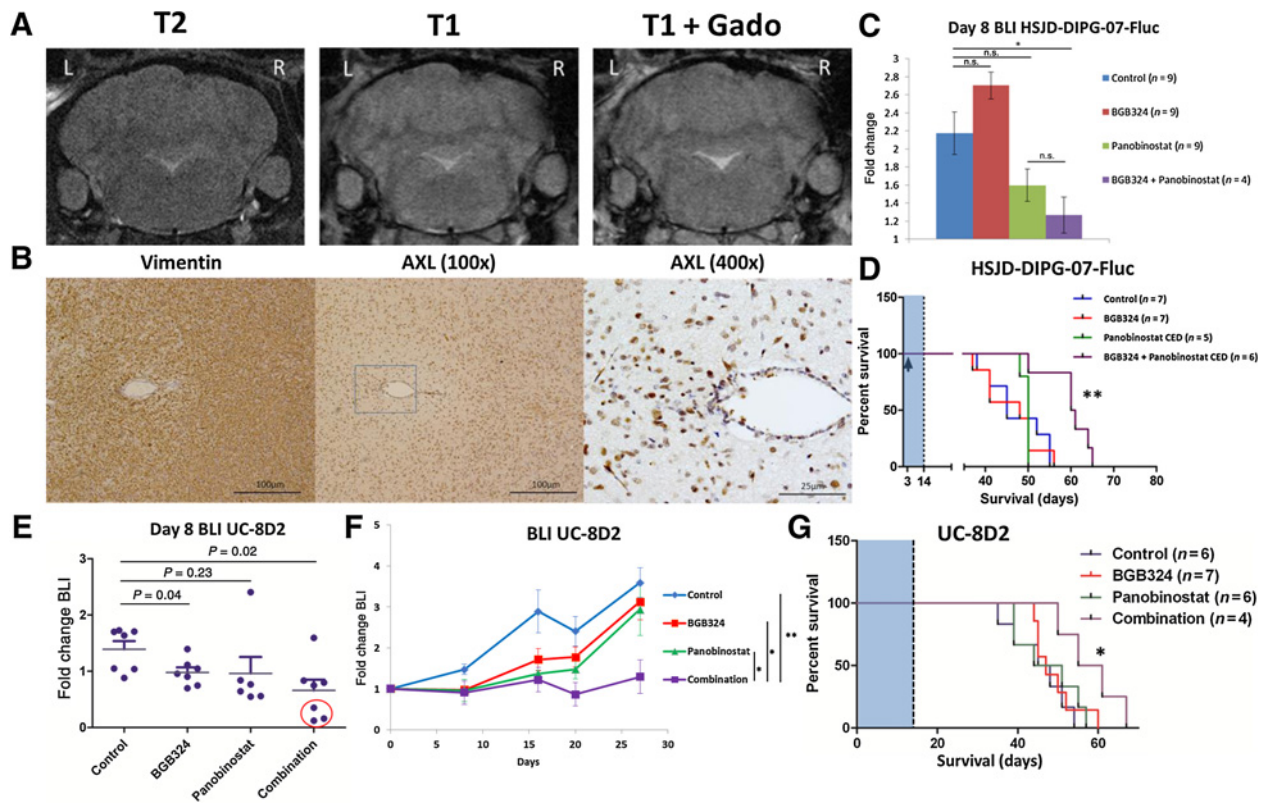


Figure 6. BGB324 and panobinostat treatment of DIPG xenograft and allograft models. **A**, MRI of the brain of mice carrying HSJD-DIPG-07-Fluc xenografts 6 weeks after injection, showing no contrast enhancement in the tumor-bearing pons. **B**, IHC staining of AXL and human vimentin in the pons of HSJD-DIPG-07 xenograft-bearing mice (see also Supplementary Fig. S1B). **C**, BLI of HSJD-DIPG-07-Fluc xenograft-bearing mice 8 days after start of treatment with BGB324 150 mg/kg/day orally and/or panobinostat 10 mg/kg/day (formulation A) intraperitoneally on days 1 to 4. Results are shown as fold change in bioluminescent signal intensity compared with baseline [* , $P < 0.05$ (independent t test)]. **D**, Survival curves of HSJD-DIPG-07-Fluc xenograft-bearing mice treated with vehicle or BGB324 150 mg/kg/day orally for 14 days (blue field) with panobinostat via CED on day 3 [arrow; ** , $P < 0.01$ (log-rank test of combination versus any other group)]. **E**, BLI of UC-8D2 allograft bearing mice 8 days after start of treatment with BGB324 150 mg/kg/day p.o. and/or panobinostat 10 mg/kg/day (formulation B) i.p. on days 1 to 5. Results are shown as fold change in bioluminescence signal intensity compared with baseline. **F**, Longitudinal BLI data of the hindbrain of UC-8D2 allograft-bearing mice treated as in **E** on days 1 to 5 and 11 to 13 (* , $P < 0.05$; ** , $P < 0.01$). **G**, Survival curves of UC-8D2 allograft bearing mice treated as in **F**. Blue area indicates treatment period [* , $P < 0.05$ (log-rank test of combination vs any other group)].

to develop an effective clinical treatment regimen. In this manuscript, we present the combination of the AXL inhibitor BGB324 and panobinostat as a novel therapeutic strategy for the treatment of DIPG. We show that AXL is highly upregulated in DIPG and strongly correlated to the mesenchymal gene expression profile of these tumors, which could be attenuated in primary DIPG cultures by the specific AXL inhibitor BGB324. Consequently, shRNA-mediated knockdown of AXL, as well as pharmacologic AXL inhibition, abrogated the invasive capacities of primary DIPG cells, an important characteristic of mesenchymal tumor cells.

We further demonstrate a synergistic antitumor effect of BGB324 and panobinostat on DIPG cells. It is noteworthy that monotherapy with either drug was not selectively toxic to H3K27M mutated cells, whereas synergy between the two drugs was only seen in H3K27M mutant cells. Importantly, treatment of DIPG cells with BGB324 and structurally distinct HDAC inhibitors resulted in a synergistic antitumor effect as well, although less strong than that observed with panobinostat, demonstrating that the synergy is a result of HDAC inhibition rather than off-target effects of panobinostat. Treatment of patient-derived DIPG cells with panobinostat strongly decreased the levels of master transcriptional regulators of the mesenchymal tran-

sition, such as ZEB1/2 and SNAIL/SLUG, and attenuated the mesenchymal gene expression pattern, an effect that was enhanced by the addition of BGB324. The decrease in cell migration and invasion that we observed upon combined treatment with BGB324 and panobinostat further supports the reversal of the mesenchymal phenotype of DIPG cells. In addition, we observed a sharp decrease in expression levels of SOX2 and its target genes after treatment of DIPG neurospheres with BGB324 and panobinostat, implicating a direct connection between mesenchymal and stem cell characteristics of DIPG cells as described for GBM and other types of cancer (7–13, 45–47). Correspondingly, we observed an ectodermal shift in gene expression pattern of DIPG cells, with upregulation of genes associated with neuronal differentiation. Besides the changes in gene expression described above, combined treatment with BGB324 and panobinostat downregulated the expression of genes associated with radiation-induced DNA damage repair, resulting in accumulation of DSBs in DIPG cells treated with these drugs after exposure to radiation. On the basis of the strong downregulation of TP53 in p53^{WT} HSJD-DIPG-07 cells compared with p53^{mut} JHH-DIPG-01 cells, there might be differences in radiosensitization of DIPG cells by BGB324 and panobinostat, based on the mutational status of p53, although the precise

mechanisms by which this would occur remain to be elucidated. The precise molecular processes responsible for the inhibition of DNA damage repair upon reversal of the mesenchymal transition by AXL/HDAC inhibition are yet to be elucidated, and form a relevant area for future research. Nonetheless, this is most likely a multifactorial process, involving downregulation of well-known key players in DNA damage repair, such as FANCD2, TP53, and RAD51, and more indirect mechanisms downstream of important mesenchymal transcription factors such as ZEB1 and β -catenin (48–51). Consequently, AXL/HDAC inhibition sensitized patient-derived DIPG neurospheres to fractionated radiation, producing strong triple antitumor synergy. Although panobinostat monotherapy already functioned as a radiosensitizer in our assays, complete obliteration of neurospheres only occurred when panobinostat and irradiation were combined with BGB324.

As an intact BBB is thought to be one of the major obstacles in the treatment of DIPG, and a common cause of therapy failure, we investigated the influence of the BBB on BGB324 brain bioavailability. Importantly, we demonstrated the capacity of BGB324 to cross the BBB and achieve pharmacologically active concentrations in the (mouse) brain. Previous research has shown that panobinostat is capable of crossing the BBB *in vivo*, ensuring that both compounds of our combination therapy can reach the tumor site (20, 52). Although *in vivo* trials to determine therapeutic efficacy of the combination of BGB324 and panobinostat in DIPG xenografts and allografts were hampered by toxicity issues with systemically administered panobinostat, we demonstrate significant growth inhibition (77%) of HSJD-DIPG-07 xenografts in mice treated with both drugs, whereas monotherapy did not have a significant impact on tumor growth. These toxicity issues are encountered frequently in mouse models despite the fact that panobinostat is tolerated in humans. Furthermore, the identified synergy between BGB324 and panobinostat may allow clinicians to reduce the panobinostat dose in patients, thereby limiting side effects. Experiments were further impeded by differences in panobinostat pharmacokinetics between mice and men. Because of the short half-life of panobinostat in mice (1.37h; ref. 52), high doses have to be administered to observe any effect in human xenografts or murine allografts. These high doses will produce off-target effects and related side effects, whereas the tumor cells are not continuously exposed to effective concentrations of panobinostat, thereby diminishing its efficacy. In humans, on the contrary, panobinostat has a half-life of ~29 hours (53), allowing for stable plasma concentrations and a more continuous exposure of tumor cells to active concentrations of the drug. This creates a far more favorable balance between therapeutic effects and side effects, especially when used in combination with other therapeutic modalities that may reduce the dose of panobinostat required for efficacy. We therefore first simulated this more favorable balance by administering a single dose of panobinostat via CED to HSJD-DIPG-07-Fluc xenograft-bearing mice, thereby eliminating systemic side effects and reducing the stress to the animals. Although treatment of these mice with panobinostat CED alone did not significantly improve survival, the concurrent administration of BGB324 with a single dose of panobinostat via CED significantly increased their median survival from 45 to 61 days. Although only a modest increase in survival, this benefit was achieved with a single dose of panobinostat, whereas panobinostat can be administered multiple times via CED in clinical trials. To reduce the toxicity of systemically administered panobinostat observed in the experiment on HSJD-DIPG-07-Fluc xeno-

graft-bearing mice, we changed the formulation of panobinostat in subsequent experiments. This treatment regimen was tolerated better by the mice, as evidenced by the reduction in weight loss and improved recovery after cessation of panobinostat treatment. Moreover, this formulation showed a stronger antitumor effect, even resulting in objective responses and partial remissions, demonstrating that systemic treatment is feasible and capable of treating DIPG xenograft and allograft models. Importantly, we did not yet perform *in vivo* experiments incorporating radiotherapy in our treatment regimen, which is expected to increase the therapeutic efficacy even further.

Altogether, our results demonstrate that combined AXL and HDAC inhibition has a synergistic antitumor effect on *in vitro* and in relevant *in vivo* models of DIPG in a H3K27M mutation-specific manner, which can be further increased by the addition of another treatment modality, such as radiotherapy. Moreover, the reversal of the mesenchymal phenotype, as well as the sharp decrease in expression of genes involved in stem cell maintenance and DNA repair and their subsequent radiosensitizing effect on DIPG cells induced by this combination therapy encourage the exploration of AXL/HDAC inhibition as a potential part of a future multimodal treatment strategy for DIPG.

Disclosure of Potential Conflicts of Interest

This study has been fully sponsored by the Semmy Foundation (<http://www.stichtingsemmy.nl>), a nonprofit organization that funds DIPG research.

BGB324 was provided by BergenBio. BergenBio was not involved in the design, execution, or analysis of the experiments and did not participate in writing the manuscript.

Authors' Contributions

Conception and design: M.H. Meel, G.J.L. Kaspers, E. Hulleman

Development of methodology: M.H. Meel, D.S. Metselaar, A.C.P. Sewing, P. Waranecki, T. Lagerweij, T.N. Phoenix, O. van Tellingen, E. Hulleman

Acquisition of data (provided animals, acquired and managed patients, provided facilities, etc.): M.H. Meel, M.C. de Gooijer, D.S. Metselaar, A.C.P. Sewing, P. Waranecki, M. Breur, T. Lagerweij, E.H. Raabe, M. Bugiani, O. van Tellingen

Analysis and interpretation of data (eg, statistical analysis, biostatistics, computational analysis): M.H. Meel, M.C. de Gooijer, D.S. Metselaar, M. Breur, T. Lagerweij, J.W.R. Twisk, J. Koster, M. Bugiani, O. van Tellingen, E. Hulleman

Writing, review, and/or revision of the manuscript: M.H. Meel, M.C. de Gooijer, D.S. Metselaar, M. Breur, J.W.R. Twisk, J. Koster, E.H. Raabe, M. Bugiani, D.G. van Vuurden, G.J.L. Kaspers, E. Hulleman

Administrative, technical, or material support (i.e., reporting or organizing data, constructing databases): K. Zwaan, P. Waranecki, L. C.M. Buil, T. Lagerweij, L.E. Wedekind, J. Koster, R. Hashizume, T.N. Phoenix, E. Hulleman

Study supervision: G.J.L. Kaspers, E. Hulleman

Other (provided disease models (human DIPG cells): A. Montero-Carcaboso

Other (generation of IUE DIPG mouse model cell lines): T.N. Phoenix

Acknowledgments

We would like to thank Professor Böcker from the Klinikum der Universität München, for generously providing us with the lentiviral hTERT construct. We would also like to express our gratitude to all the patients and their parents who have participated in biopsy or autopsy studies that enabled us to develop the models necessary for this study. All research described has been funded by the Semmy Foundation (<http://www.stichtingsemmy.nl>).

The costs of publication of this article were defrayed in part by the payment of page charges. This article must therefore be hereby marked *advertisement* in accordance with 18 U.S.C. Section 1734 solely to indicate this fact.

Received October 28, 2019; revised January 4, 2020; accepted March 6, 2020; published first March 12, 2020.

References

- Veldhuijzen van Zanten SEM, Lane A, Heymans MW, Baugh J, Chaney B, Hoffman LM, et al. External validation of the diffuse intrinsic pontine glioma survival prediction model: a collaborative report from the International DIPG Registry and the SIOPE DIPG Registry. *J Neurooncol* 2017;134:231–40.
- Robison NJ, Kieran MW. Diffuse intrinsic pontine glioma: a reassessment. *J Neurooncol* 2014;119:7–15.
- Castel D, Philippe C, Calmon R, Le Dret L, Truffaux N, Boddaert N, et al. Histone H3F3A and HIST1H3B K27M mutations define two subgroups of diffuse intrinsic pontine gliomas with different prognosis and phenotypes. *Acta Neuropathol* 2015;130:815–27.
- Meel MH, Schaper SA, Kaspers GJL, Hulleman E. Signaling pathways and mesenchymal transition in pediatric high-grade glioma. *Cell Mol Life Sci* 2018; 75:871–87.
- Puget S, Philippe C, Bax DA, Job B, Varlet P, Junier MP, et al. Mesenchymal transition and PDGFRA amplification/mutation are key distinct oncogenic events in pediatric diffuse intrinsic pontine gliomas. *PLoS One* 2012;7:e30313.
- Halliday J, Helmy K, Pattwell SS, Pitter KL, LaPlant Q, Ozawa T, et al. In vivo radiation response of proneural glioma characterized by protective p53 transcriptional program and proneural-mesenchymal shift. *Proc Natl Acad Sci U S A* 2014;111:5248–53.
- Segerman A, Niklasson M, Haglund C, Bergström T, Jarvius M, Xie Y, et al. Clonal variation in drug and radiation response among glioma-initiating cells is linked to proneural-mesenchymal transition. *Cell Rep* 2016;17:2994–3009.
- Mahabir R, Tanino M, Elmansuri A, Wang L, Kimura T, Itoh T, et al. Sustained elevation of Snail promotes glial-mesenchymal transition after irradiation in malignant glioma. *Neuro Oncol* 2014;16:671–85.
- Siebzehnrubl FA, Silver DJ, Tugertimur B, Deleyrolle LP, Siebzehnrubl D, Sarkisian MR, et al. The ZEB1 pathway links glioblastoma initiation, invasion and chemoresistance. *EMBO Mol Med* 2013;5:1196–212.
- Singh DK, Kollipara RK, Vemireddy V, Yang XL, Sun Y, Regmi N, et al. Oncogenes activate an autonomous transcriptional regulatory circuit that drives glioblastoma. *Cell Rep* 2017;18:961–76.
- Wellner U, Schubert J, Burk UC, Schmalhofer O, Zhu F, Sonntag A, et al. The EMT-activator ZEB1 promotes tumorigenicity by repressing stemness-inhibiting microRNAs. *Nat Cell Biol* 2009;11:1487–95.
- Zhao X, Sun B, Sun D, Liu T, Che N, Gu Q, et al. Slug promotes hepatocellular cancer cell progression by increasing sox2 and nanog expression. *Oncol Rep* 2015;33:149–56.
- Zhou W, Lv R, Qi W, Wu D, Xu Y, Liu W, et al. Snail contributes to the maintenance of stem cell-like phenotype cells in human pancreatic cancer. *PLoS One* 2014;9:e87409.
- Cheng P, Phillips E, Kim SH, Taylor D, Hielscher T, Puccio L, et al. Kinome-wide shRNA screen identifies the receptor tyrosine kinase AXL as a key regulator for mesenchymal glioblastoma stem-like cells. *Stem Cell Rep* 2015; 4:899–913.
- Hutterer M, Knyazev P, Abate A, Reschke M, Maier H, Stefanova N, et al. Axl and growth arrest-specific gene 6 are frequently overexpressed in human gliomas and predict poor prognosis in patients with glioblastoma multiforme. *Clin Cancer Res* 2008;14:130–8.
- Onken J, Torka R, Korsing S, Radke J, Kremenceskaia I, Nieminen M, et al. Inhibiting receptor tyrosine kinase AXL with small molecule inhibitor BMS-777607 reduces glioblastoma growth, migration, and invasion *in vitro* and *in vivo*. *Oncotarget* 2016;7:9876–89.
- Ott M, Litzenburger UM, Sahn F, Rauschenbach KJ, Tudoran R, Hartmann C, et al. Promotion of glioblastoma cell motility by enhancer of zeste homolog 2 (EZH2) is mediated by AXL receptor kinase. *PLoS One* 2012; 7:e47663.
- Vouri M, An Q, Birt M, Pilkington GJ, Hafizi S. Small molecule inhibition of Axl receptor tyrosine kinase potently suppresses multiple malignant properties of glioma cells. *Oncotarget* 2015;6:16183–197.
- Holland SJ, Pan A, Franci C, Hu Y, Chang B, Li W, et al. R428, a selective small molecule inhibitor of Axl kinase, blocks tumor spread and prolongs survival in models of metastatic breast cancer. *Cancer Res* 2010;70:1544–54.
- Grasso CS, Tang Y, Truffaux N, Berlow NE, Liu L, Debily MA, et al. Functionally defined therapeutic targets in diffuse intrinsic pontine glioma. *Nat Med* 2015;21: 555–59.
- DI Fazio P, Montalbano R, Quint K, Alinger B, Kemmerling R, Kiesslich T, et al. The pan-deacetylase inhibitor panobinostat modulates the expression of epithelial-mesenchymal transition markers in hepatocellular carcinoma models. *Oncol Lett* 2013;5:127–34.
- Rhodes LV, Tate CR, Segar HC, Burks HE, Phamduy TB, Hoang V, et al. Suppression of triple-negative breast cancer metastasis by pan-DAC inhibitor panobinostat via inhibition of ZEB family of EMT master regulators. *Breast Cancer Res Treat* 2014;145:593–604.
- Venkatesh HS, Johung TB, Caretti V, Noll A, Tang Y, Nagaraja S, et al. Neuronal activity promotes glioma growth through neuropilin-3 secretion. *Cell* 2015;161: 803–16.
- Jansen MH, Lagerweij T, Sewing AC, Vuğts DJ, van Vuurden DG, Molthoff CF, et al. Bevacizumab targeting diffuse intrinsic pontine glioma: results of 89Zr-Bevacizumab PET imaging in brain tumor models. *Mol Cancer Ther* 2016;15: 2166–74.
- Taylor IC, Hütt-Cabezas M, Brandt WD, Kambhampati M, Nazarian J, Chang HT, et al. Disrupting NOTCH slows diffuse intrinsic pontine glioma growth, enhances radiation sensitivity, and shows combinatorial efficacy with bromodomain inhibition. *J Neuropathol Exp Neurol* 2015;74:778–90.
- Hashizume R, Andor N, Ihara Y, Lerner R, Gan H, Chen X, et al. Pharmacologic inhibition of histone demethylation as a therapy for pediatric brainstem glioma. *Nat Med* 2014;20:1394–96.
- Meel MH, de Gooijer MC, Guillén Navarro M, Waranecki P, Breur M, Buil LCM, et al. MELK inhibition in diffuse intrinsic pontine glioma. *Clin Cancer Res* 2018; 24:5645–57.
- Patel SK, Hartley RM, Wei X, Furnish R, Escobar-Riquelme F, Bear H, et al. Generation of diffuse intrinsic pontine glioma mouse models by brainstem targeted in utero electroporation. *Neuro Oncol* 2019;22:381–92.
- Vinci M, Burford A, Molinari V, Kessler K, Popov S, Clarke M, et al. Functional diversity and cooperativity between subclonal populations of pediatric glioblastoma and diffuse intrinsic pontine glioma cells. *Nat Med* 2018;24:1204–15.
- Peferoen LA, Breur M, van de Berg S, Peferoen-Baert R, Boddeke EH, van der Valk P, et al. Ageing and recurrent episodes of neuroinflammation promote progressive experimental autoimmune encephalomyelitis in Biozzi ABH mice. *Immunology* 2016;149:146–56.
- Depienne C, Bugiani M, Dupuits C, Galanaud D, Touitou V, Postma N, et al. Brain white matter oedema due to CIC-2 chloride channel deficiency: an observational analytical study. *Lancet Neurol* 2013;12:659–68.
- Chou TC, Talaly P. A simple generalized equation for the analysis of multiple inhibitions of Michaelis-Menten kinetic systems. *J Biol Chem* 1977;252: 6438–42.
- Larson JD, Kasper LH, Paugh BS, Jin H, Wu G, Kwon CH, et al. Histone H3.3 K27M accelerates spontaneous brainstem glioma and drives restricted changes in bivalent gene expression. *Cancer Cell* 2019;35:140–55.
- Paugh BS, Broniscer A, Qu C, Miller CP, Zhang J, Tatevossian RG, et al. Genome-wide analyses identify recurrent amplifications of receptor tyrosine kinases and cell-cycle regulatory genes in diffuse intrinsic pontine glioma. *J Clin Oncol* 2011; 29:3999–4006.
- Harris LW, Lockstone HE, Khaitovich P, Weickert CS, Webster MJ, Bahn S, et al. Gene expression in the prefrontal cortex during adolescence: implications for the onset of schizophrenia. *BMC Med Genomics* 2009;2:28.
- Roth RB, Hevezi P, Lee J, Willhite D, Lechner SM, Foster AC, et al. Gene expression analyses reveal molecular relationships among 20 regions of the human CNS. *Neurogenetics* 2006;7:67–80.
- Verhaak RG, Hoadley KA, Purdom E, Wang V, Qi Y, Wilkerson MD, et al. Integrated genomic analysis identifies clinically relevant subtypes of glioblastoma characterized by abnormalities in PDGFRA, IDH1, EGFR, and NF1. *Cancer Cell* 2010;17:98–110.
- Silveira AB, Kasper LH, Fan Y, Jin H, Wu G, Shaw TL, et al. H3.3 K27M depletion increases differentiation and extends latency of diffuse intrinsic pontine glioma growth *in vivo*. *Acta Neuropathol* 2019;137:637–55.
- Sadahiro H, Kang KD, Gibson JT, Minata M, Yu H, Shi J, et al. Activation of the receptor tyrosine kinase AXL regulates the immune microenvironment in glioblastoma. *Cancer Res* 2018;78:3002–13.
- Nagaraja S, Vitanza NA, Woo PJ, Taylor KR, Liu F, Zhang L, et al. Transcriptional dependencies in diffuse intrinsic pontine glioma. *Cancer Cell* 2017;31: 635–52.
- Ben-Porath I, Thomson MW, Carey VJ, Ge R, Bell GW, Regev A, et al. An embryonic stem cell-like gene expression signature in poorly differentiated aggressive human tumors. *Nat Genet* 2008;40:499–507.
- Le MT, Xie H, Zhou B, Chia PH, Rizk P, Um M, et al. MicroRNA-125b promotes neuronal differentiation in human cells by repressing multiple targets. *Mol Cell Biol* 2009;29:5290–305.

43. Pala A, Karpel-Massler G, Kast RE, Wirtz CR, Halatsch ME. Epidermal to mesenchymal transition and failure of EGFR-targeted therapy in glioblastoma. *Cancers* 2012;4:523–30.
44. de Gooijer MC, Zhang P, Weijer R, Buil LCM, Beijnen JH, van Tellingen O, et al. The impact of P-glycoprotein and breast cancer resistance protein on the brain pharmacokinetics and pharmacodynamics of a panel of MEK inhibitors. *Int J Cancer* 2017;142:381–91.
45. Drachsler M, Kleber S, Mateos A, Volk K, Mohr N, Chen S, et al. CD95 maintains stem cell-like and non-classical EMT programs in primary human glioblastoma cells. *Cell Death Dis* 2016;7:e2209.
46. Chow KH, Park HJ, George J, Yamamoto K, Gallup AD, Graber JH, et al. S100A4 Is a biomarker and regulator of glioma stem cells that is critical for mesenchymal transition in glioblastoma. *Cancer Res* 2017;77:536073.
47. Minata M, Audia A, Shi J, Lu S, Bernstock J, Pavlyukov MS, et al. Phenotypic plasticity of invasive edge glioma stem-like cells in response to ionizing radiation. *Cell Rep* 2019;26:1893–905.
48. Nepal M, Che R, Ma C, Zhang J, Fei P. FANCD2 and DNA damage. *Int J Mol Sci* 2017;18. doi: 10.3390/ijms18081804.
49. Sato K, Shimomuki M, Katsuki Y, Takahashi D, Kobayashi W, Ishiai M, et al. FANCI-FANCD2 stabilizes the RAD51-DNA complex by binding RAD51 and protects the 5'-DNA end. *Nucleic Acids Res* 2016;44:10758–71.
50. Wang C, Jin H, Wang N, Fan S, Wang Y, Zhang Y, et al. Gas6/Axl axis contributes to chemoresistance and metastasis in breast cancer through Akt/GSK-3beta/beta-catenin signaling. *Theranostics* 2016;6:1205–19.
51. Zhang X, Zhang Z, Zhang Q, Zhang Q, Sun P, Xiang R, et al. ZEB1 confers chemotherapeutic resistance to breast cancer by activating ATM. *Cell Death Dis* 2018;9:57.
52. Garbes L, Riessland M, Hölker I, Heller R, Hauke J, Tränkle C, et al. LBH589 induces up to 10-fold SMN protein levels by several independent mechanisms and is effective even in cells from SMA patients non-responsive to valproate. *Hum Mol Genet* 2009;18:3645–58.
53. Sharma S, Witteveen PO, Lolkema MP, Hess D, Gelderblom H, Hussain SA, et al. A phase I, open-label, multicenter study to evaluate the pharmacokinetics and safety of oral panobinostat in patients with advanced solid tumors and varying degrees of renal function. *Cancer Chemother Pharmacol* 2015; 75:87–95.